

Exhibit 14

Part 3

and 30 and are repeated here:

$$J_p = -q\mu_p p \nabla \phi_p$$

$$J_n = -q\mu_n n \nabla \phi_n$$

Since J_p , q , μ_p , and p are positive, the hole imref decreases monotonically to the right as shown in Fig. 18a. Similarly, the electron imref increases monotonically to the left. Thus everywhere the separation of the imrefs must be less than or equal to the applied voltage, and therefore³⁰

$$pn \leq n_i^2 \exp\left(\frac{qV}{kT}\right) \quad (57)$$

even under the high-injection condition. Note also that the foregoing argument does not depend on recombination in the depletion region. As long as recombination takes place somewhere, currents will flow.

To illustrate the high-injection case, we present in Fig. 22 plots of numerical results for intrinsic Fermi level (ψ), imrefs (ϕ_n and ϕ_p), and carrier concentrations for a silicon p - n step junction with the following parameters: $N_A = 10^{18} \text{ cm}^{-3}$, $N_D = 10^{16} \text{ cm}^{-3}$, $\tau_n = 3 \times 10^{-10} \text{ s}$, and $\tau_p = 8.4 \times 10^{-10} \text{ s}$. The current densities in Fig. 22a, b, and c are 10 , 10^3 , and 10^4 A/cm^2 . At 10 A/cm^2 the diode is in the low-injection regime. Almost all of the potential drop occurs across the junction. The hole concentration on the n side is small compared to the electron concentration. At 10^3 A/cm^2 the electron concentration near the junction exceeds the donor concentration appreciably. An ohmic potential drop appears on the n side. At

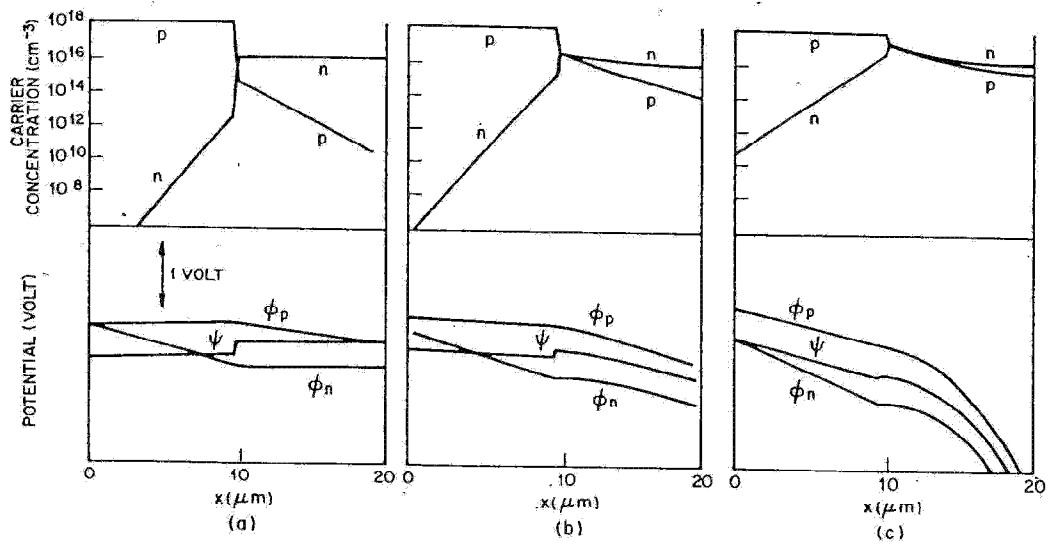


Fig. 22 Carrier concentrations, intrinsic Fermi level (ψ) and imrefs for a Si p - n junction operated at different current densities. (a) 10 A/cm^2 . (b) 10^3 A/cm^2 . (c) 10^4 A/cm^2 . (After Gummel, Ref. 30.)

10^4 A/cm^2 we have very high injection; the potential drop across the junction is insignificant compared to ohmic drops on both sides. Even though only the center region of diode is shown in Fig. 22, it is apparent that the separation of the imrefs at the junction is less than or equal to the difference in the hole imref to the left of the junction and the electron imref to the right of the junction for all forward-bias levels.

From Fig. 22b and c, the carrier densities at the n side of the junction are comparable ($n \approx p$). Substituting this condition in Eq. 57, we obtain $p_n(x = x_n) \approx n_i \exp(qV/2kT)$. The current then becomes roughly proportional to $\exp(qV/2kT)$, as shown in Fig. 21, curve (c).

At high-injection levels we should consider another effect associated with the finite resistivity in the quasi-neutral regions of the junction. This resistance absorbs an appreciable amount of the voltage drop between the diode terminals. This effect is shown in Fig. 21, curve (d). The series resistance effect can be substantially reduced by the use of epitaxial materials.

2.4.4 Diffusion Capacitance

The depletion-layer capacitance considered previously accounts for most of the junction capacitance when the junction is reverse-biased. When forward-biased, there is in addition a significant contribution to junction capacitance from the rearrangement of minority carrier density, the so-called diffusion capacitance. When a small ac signal is applied to a junction that is forward-biased to a voltage V_0 and current density J_0 , the total voltage and current are defined by

$$\begin{aligned} V(t) &= V_0 + V_1 e^{j\omega t} \\ J(t) &= J_0 + J_1 e^{j\omega t} \end{aligned} \quad (58)$$

where V_1 and J_1 are the small-signal amplitude of the voltage and current density, respectively. The electron and hole densities at the depletion region boundaries can be obtained from Eqs. 32 and 33 by using $(V_0 + V_1 e^{j\omega t})$ instead of V . The small-signal ac component of the hole density is given by

$$\bar{p}_n(x, t) = p_{n1}(x) e^{j\omega t} \quad (59)$$

We obtain for $V_1 \ll V_0$,

$$\begin{aligned} p_n &= p_{n0} \exp\left[\frac{q(V_0 + V_1 e^{j\omega t})}{kT}\right] \\ &\approx p_{n0} \exp\left(\frac{qV_0}{kT}\right) + \frac{p_{n0} q V_1}{kT} \exp\left(\frac{qV_0}{kT}\right) e^{j\omega t}. \end{aligned} \quad (60)$$

A similar expression is obtained for the electron density. The first term in Eq. 60 is the dc component, and the second term is the small-signal ac

component at the depletion-layer boundary $[p_{n1}(x_n)e^{j\omega t}]$. Substituting p_n into the continuity equation (Eq. 97 of Chapter 1 with $G_p = 0$) yields

$$j\omega\tilde{p}_n = -\frac{\tilde{p}_n}{\tau_p} + D_p \frac{\partial^2 \tilde{p}_n}{\partial x^2}$$

or

$$\frac{\partial^2 \tilde{p}_n}{\partial x^2} - \frac{\tilde{p}_n}{D_p \tau_p / (1 + j\omega \tau_p)} = 0. \quad (61)$$

Equation 61 is identical to Eq. 39 if the carrier lifetime is expressed as

$$\tau_p^* = \frac{\tau_p}{1 + j\omega \tau_p}. \quad (62)$$

We can then obtain the alternating current density from Eq. 44 by making the appropriate substitutions:

$$J_1 = \frac{qV_1}{kT} \left[\frac{qD_p p_{n0}}{L_p \sqrt{1 + j\omega \tau_p}} + \frac{qD_n n_{p0}}{L_n \sqrt{1 + j\omega \tau_n}} \right] \exp\left(\frac{qV_0}{kT}\right). \quad (63)$$

Equation 63 leads directly to the ac admittance:

$$Y \equiv \frac{J_1}{V_1} = G_d + j\omega C_d. \quad (64)$$

For relatively low frequencies ($\omega\tau_p, \omega\tau_n \ll 1$), the diffusion conductance G_{d0} is given by

$$G_{d0} = \frac{q}{kT} \left(\frac{qD_p p_{n0}}{L_p} + \frac{qD_n n_{p0}}{L_n} \right) e^{qV_0/kT} \quad \text{mho/cm}^2 \quad (65)$$

which has exactly the same value obtained by differentiating Eq. 44. The

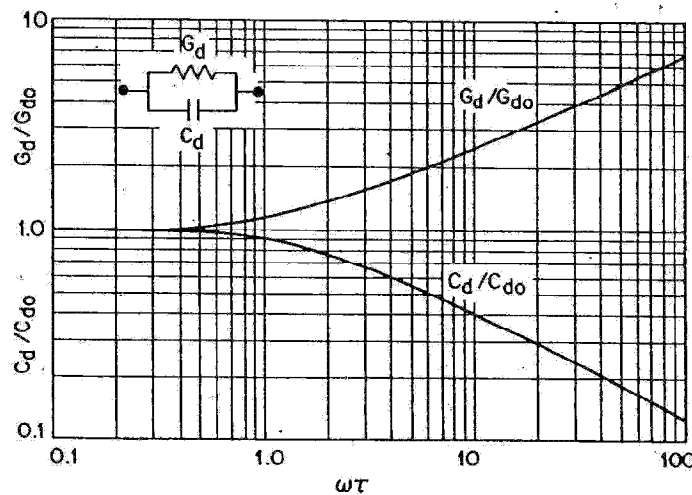


Fig. 23 Normalized diffusion conductance and diffusion capacitance versus $\omega\tau$. Insert shows the equivalent circuit of a p-n junction under forward bias.

low-frequency diffusion capacitance C_{d0} is given by

$$C_{d0} = \frac{q}{kT} \left(\frac{qL_p p_{no}}{2} + \frac{qL_n n_{po}}{2} \right) e^{qV_0/kT} \quad \text{F/cm}^2. \quad (66)$$

The frequency dependence of the conductance and capacitance is shown in Fig. 23 as a function of the normalized frequency $\omega\tau$ where only one term in Eq. 63 is considered (e.g., the term contains p_{no} if $p_{no} \gg n_{po}$). The insert shows the equivalent circuit of the ac admittance. It is clear from Fig. 23 that the diffusion capacitance decreases with increasing frequency. For large frequencies, C_d is approximately $(\omega)^{-1/2}$. The diffusion capacitance, however, increases with the direct current level ($\sim e^{qV_0/kT}$). For this reason, C_d is especially important at low frequencies and under forward-bias conditions.

2.5 JUNCTION BREAKDOWN³¹

When a sufficiently high field is applied to a p - n junction, the junction "breaks down" and conducts a very large current. There are basically three breakdown mechanisms: thermal instability, tunneling effect, and avalanche multiplication. We consider the first two mechanisms briefly, and discuss avalanche multiplication in detail.

2.5.1 Thermal Instability

Breakdown due to thermal instability is responsible for the maximum dielectric strength in most insulators at room temperature, and is also a major effect in semiconductors with relatively small bandgaps (e.g., Ge). Because of the heat dissipation caused by the reverse current at high reverse voltage, the junction temperature increases. This temperature increase, in turn, increases the reverse current in comparison with its value at lower voltages. The temperature effect³² on reverse current-voltage characteristics is shown in Fig. 24. In this figure the reverse currents J_s are represented by a family of horizontal lines. Each line represents the current at a constant junction temperature, and the current varies as $T^{3+\gamma/2} \exp(-E_g/kT)$, as discussed previously. The heat dissipation hyperbolas which are proportional to the I - V product are shown as straight lines in the log-log plot. These lines also correspond to curves of constant junction temperature. The reverse current-voltage characteristic of the junction is obtained by joining the intersection points of the curves of constant junction temperature. Because of the heat dissipation at high reverse voltage, the characteristic shows a negative differential resistance. In this case the diode will be destroyed unless some special measure such as a large series-limiting resistor is used. This effect is called thermal instability. The voltage V_U is called the turnover voltage. For p - n junctions

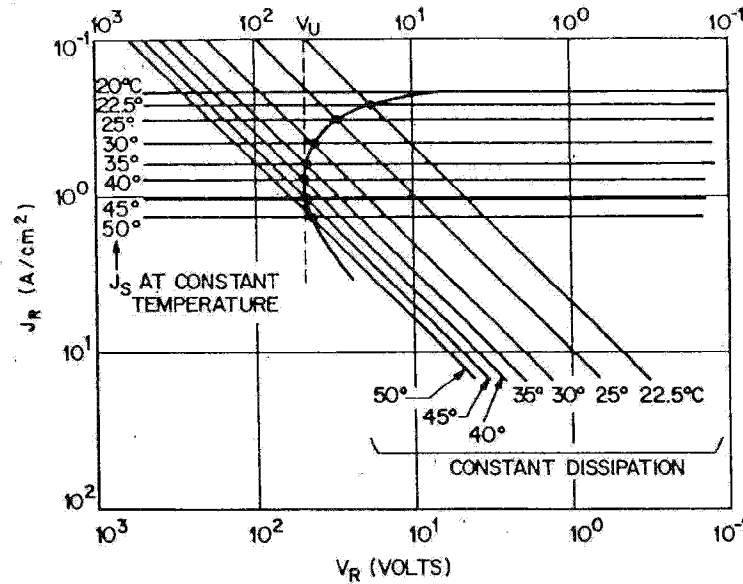


Fig. 24 Reverse current-voltage characteristics of thermal breakdown, where V_U is the turnover voltage. (Note: Direction of coordinate increases are opposite to usual conventions.) (After Strutt, Ref. 32.)

with relatively large saturation currents (e.g., Ge), the thermal instability is important at room temperature. At very low temperatures, however, thermal instability becomes less important compared with other mechanisms.

2.5.2 Tunneling Effect

We next consider the tunneling effect. It is well known that for a one-dimensional square energy barrier with barrier height E_0 and thickness W , the quantum-mechanical transmission probability T_t is given by³³

$$T_t = \left[1 + \frac{E_0^2 \sinh^2 \kappa W}{4E(E_0 - E)} \right]^{-1} \quad (67)$$

with

$$\kappa \equiv \sqrt{\frac{2m(E_0 - E)}{\hbar^2}}$$

where E is the energy of the carrier. The probability decreases monotonically with decreasing E . When $\kappa W \gg 1$, the probability becomes

$$T_t \approx \frac{16E(E_0 - E)}{E_0^2} \exp(-2\kappa W). \quad (67a)$$

A similar expression has been obtained for p - n junctions. The detailed mathematical treatment is given in Chapter 9. The tunneling current density

is given by³¹

$$J_t = \frac{\sqrt{2m^*} q^3 \mathcal{E} V}{4\pi^2 \hbar^2 E_g^{1/2}} \exp\left(-\frac{4\sqrt{2m^*} E_g^{3/2}}{3q\mathcal{E}\hbar}\right) \quad (68)$$

where \mathcal{E} is the electric field at the junction, E_g the bandgap, V the applied voltage, and m^* the effective mass.

When the field approaches 10^6 V/cm in Ge and Si, significant current begins to flow by means of the band-to-band tunneling process. To obtain such a high field, the junction must have relatively high impurity concentrations on both the p and n sides. The mechanism of breakdown for Si and Ge junctions with breakdown voltages less than about $4E_g/q$ is found to be due to the tunneling effect. For junctions with breakdown voltages in excess of $6E_g/q$, the mechanism is caused by the avalanche multiplication. At voltages between 4 and $6E_g/q$, the breakdown is due to a mixture of both avalanche and tunneling. Since the energy bandgaps E_g in Ge, Si, and GaAs decrease with increasing temperature (refer to Chapter 1), the breakdown voltage in these semiconductors due to the tunneling effect has a negative temperature coefficient; that is, the voltage decreases with increasing temperature. This is because a given breakdown current J_t can be reached at smaller reverse voltages (or fields) at higher temperatures, Eq. 68. A typical example is shown in Fig. 25. This temperature effect is generally used to distinguish the tunneling mechanism from the avalanche mechanism, which has a positive temperature coefficient; that is, the breakdown voltage increases with increasing temperature.

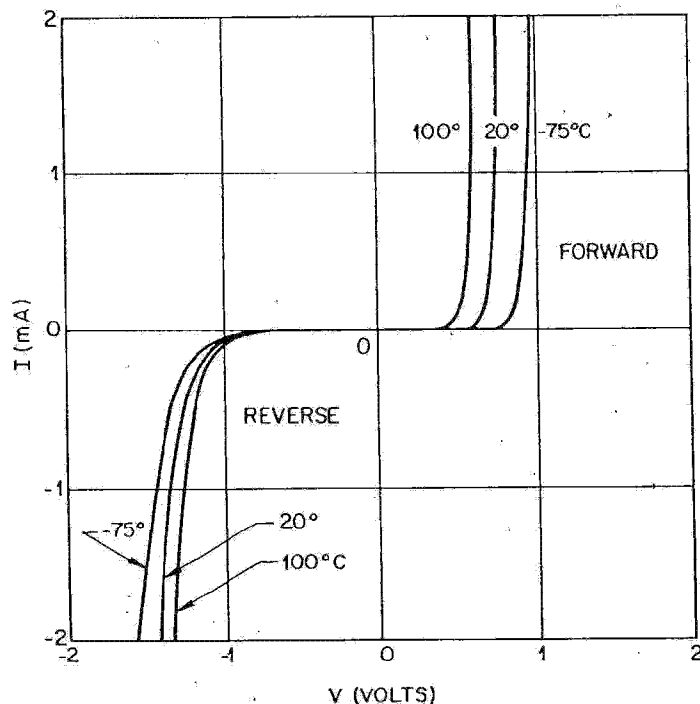


Fig. 25 Current-voltage characteristics of tunneling breakdown. (After Strutt, Ref. 32.)

2.5.3 Avalanche Multiplication

Avalanche multiplication (or impact ionization) is the most important mechanism in junction breakdown, since the avalanche breakdown voltage imposes an upper limit on the reverse bias for most diodes, on the collector voltage of bipolar transistors (Chapter 3) and on the drain voltages of MESFETs (Chapter 6) and MOSFETs (Chapter 8). In addition, the impact ionization mechanism can be used to generate microwave power, as in IMPATT devices (Chapter 10), and to detect optical signals, as in avalanche photodetectors (Chapter 13).

We first derive the basic ionization integral which determines the breakdown condition. Assume that a current I_{po} is incident at the left-hand side of the depletion region with width W . If the electric field in the depletion region is high enough that electron-hole pairs are generated by the impact ionization process, the hole current I_p will increase with distance through the depletion region and reaches a value $M_p I_{po}$ at W . Similarly, the electron current I_n will increase from $x = W$ to $x = 0$. The total current $I (= I_p + I_n)$ is constant at steady state. The incremental hole current at x equals the number of electron-hole pairs generated per second in the distance dx ,

$$d(I_p/q) = (I_p/q)(\alpha_p dx) + (I_n/q)(\alpha_n dx) \quad (69)$$

or

$$dI_p/dx - (\alpha_p - \alpha_n)I_p = \alpha_n I. \quad (70)$$

The electron and hole ionization rates (α_n and α_p) have been considered in Chapter 1.

The solution* of Eq. 70 with boundary condition that $I = I_p(W) = M_p I_{po}$ is given by

$$I_p(x) = I \left\{ \frac{1}{M_p} + \int_0^x \alpha_n \exp \left[- \int_0^x (\alpha_p - \alpha_n) dx' \right] dx \right\} / \exp \left[- \int_0^x (\alpha_p - \alpha_n) dx' \right] \quad (71)$$

where M_p is the multiplication factor of holes and is defined as

$$M_p = \frac{I_p(W)}{I_p(0)}. \quad (72)$$

Equation 71 can be written as

$$1 - \frac{1}{M_p} = \int_0^W \alpha_p \exp \left[- \int_0^x (\alpha_p - \alpha_n) dx' \right] dx. \quad (73)$$

*Equation 70 has the form $y' + Py = Q$, where $y = I_p$. The standard solution is

$$y = \left[\int_0^x Q e^{\int_0^x P dx'} dx + C \right] / e^{\int_0^x P dx'}$$

where C is the constant of integration.

The avalanche breakdown voltage is defined as the voltage where M_p approaches infinity. Hence the breakdown condition is given by the ionization integral

$$\int_0^W \alpha_p \exp\left[-\int_0^x (\alpha_p - \alpha_n) dx'\right] dx = 1. \quad (74)$$

If the avalanche process is initiated by electrons instead of holes, the ionization integral is given by

$$\int_0^W \alpha_n \exp\left[-\int_x^W (\alpha_n - \alpha_p) dx'\right] dx = 1. \quad (75)$$

Equations 74 and 75 are equivalent;³⁴ that is, the breakdown condition depends only on what is happening within the depletion region and not on the carriers (or primary current) that initiate the avalanche process. The situation does not change when a mixed primary current initiates the breakdown, so either Eq. 74 or Eq. 75 gives the breakdown condition.

For semiconductors with equal ionization rates ($\alpha_n = \alpha_p = \alpha$) such as GaP, Eqs. 74 or 75 reduce to the simple expression

$$\int_0^W \alpha dx = 1. \quad (76)$$

From the breakdown conditions described above and the field dependence of the ionization rates, the breakdown voltages, maximum electric field, and depletion-layer width can be calculated. As discussed previously, the electric field and potential in the depletion layer are determined from the solutions of Poisson's equation. Depletion-layer boundaries that satisfy Eq. 74 can be obtained numerically using an iteration method. With known boundaries we obtain

$$V_B(\text{breakdown voltage}) = \frac{\mathcal{E}_m W}{2} = \frac{\epsilon_s \mathcal{E}_m^2}{2q} (N_B)^{-1} \quad (77a)$$

for one-sided abrupt junctions, and

$$V_B = \frac{2\mathcal{E}_m W}{3} = \frac{4\mathcal{E}_m^{3/2}}{3} \left(\frac{2\epsilon_s}{q}\right)^{1/2} (a)^{-1/2} \quad (77b)$$

for linearly graded junctions, where N_B is the ionized background impurity concentration of the lightly doped side, ϵ_s the semiconductor permittivity, a the impurity gradient, and \mathcal{E}_m the maximum field.

Figure 26 shows the calculated breakdown voltage³⁵ as a function of N_B for abrupt junctions in Ge, Si, $\langle 100 \rangle$ -oriented GaAs, and GaP. The experimental results are generally in good agreement with the calculated values.³⁶ The dashed lines in the figure indicate the upper limit of N_B for which the avalanche breakdown calculation is valid. This limitation is based on the criterion $6E_g/q$. Above these values the tunneling mechanism will also contribute to the breakdown process and eventually dominates.

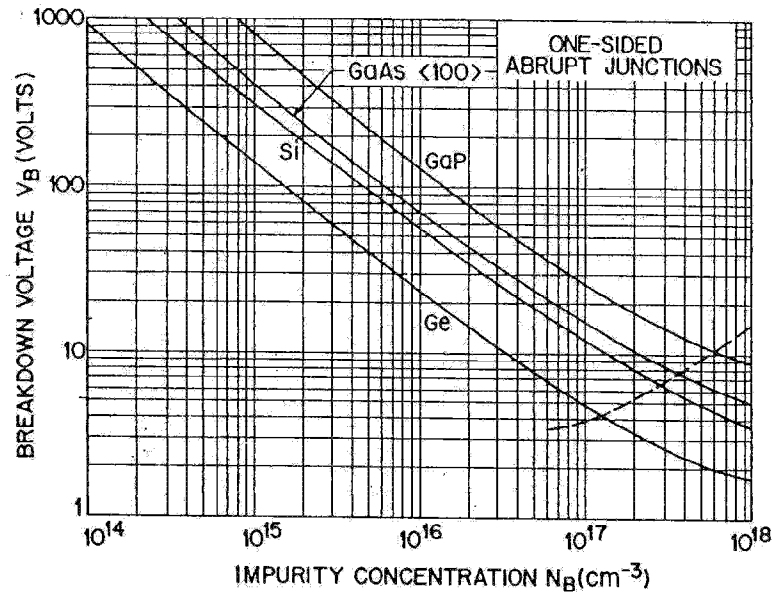


Fig. 26 Avalanche breakdown voltage versus impurity concentration for one-sided abrupt junctions in Ge, Si, <100>-oriented GaAs, and GaP. The dashed line indicates the maximum doping beyond which the tunneling mechanism will dominate the voltage breakdown characteristics. (After Sze and Gibbons, Ref. 35.)

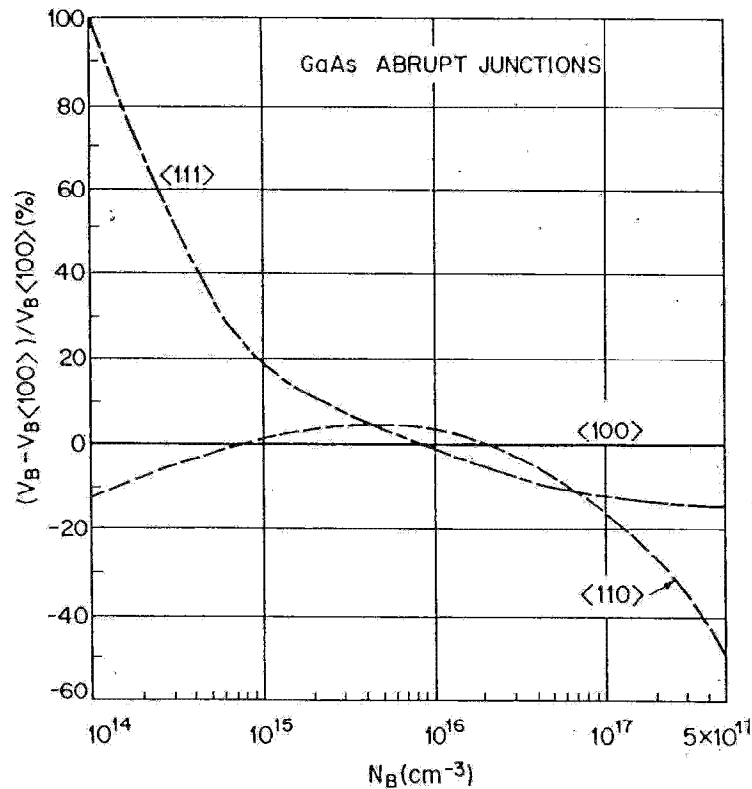


Fig. 27 Orientation dependence of avalanche breakdown voltage in one-sided abrupt GaAs junctions. (After Lee and Sze, Ref. 37.)

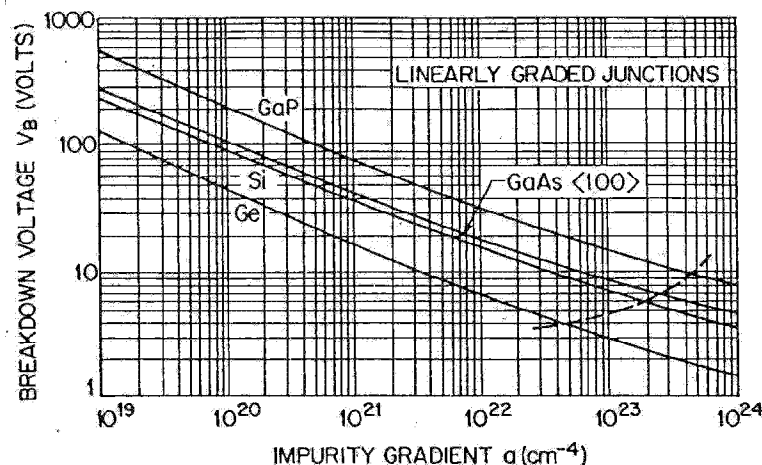


Fig. 28 Avalanche breakdown voltage versus impurity gradient for linearly graded junctions in Ge, Si, (100)-oriented GaAs, and GaP. The dashed line indicates the maximum gradient beyond which the tunneling mechanism will set in. (After Sze and Gibbons, Ref. 35.)

In GaAs, the ionization rates depend on crystal orientations (refer to Chapter 1). Figure 27 shows a comparison³⁷ of V_B in (111) and (110) orientations with respect to that in (100). Note that at around 10^{16} cm^{-3} , the breakdown voltages are essentially independent of orientations. At lower dopings, V_B in (111) becomes the largest; whereas at higher dopings, V_B in (100) is the largest.

Figure 28 shows the calculated breakdown voltage versus the impurity gradient for linearly graded junctions in these semiconductors. The dashed line indicates the upper limit of a for which the avalanche breakdown calculation is valid.

The calculated values of the maximum field \mathcal{E}_m and the depletion-layer width at breakdown for the four semiconductors above are shown³⁵ in Fig. 29 for the abrupt junctions and in Fig. 30 for the linearly graded junctions. For the Si junctions, the maximum field can be expressed as³⁸

$$\mathcal{E}_m = \frac{4 \times 10^5}{1 - \frac{1}{3} \log_{10} (N_B / 10^{16})} \quad \text{V/cm} \quad (78)$$

where N_B is in cm^{-3} .

Because of the strong dependence of the ionization rates on the field, the maximum field varies very slowly with either N_B or a . Thus as a first approximation we can assume that, for a given semiconductor, \mathcal{E}_m has a fixed value. Then from Eq. 77 we obtain $V_B \sim N_B^{-1.0}$ for abrupt junctions and $V_B \sim a^{-0.5}$ for linearly graded junctions. Figures 26 and 28 show that the foregoing patterns are generally followed. Also as expected, for a given N_B or a , the breakdown voltage increases with the energy bandgap, since the avalanche process requires band-to-band excitations.

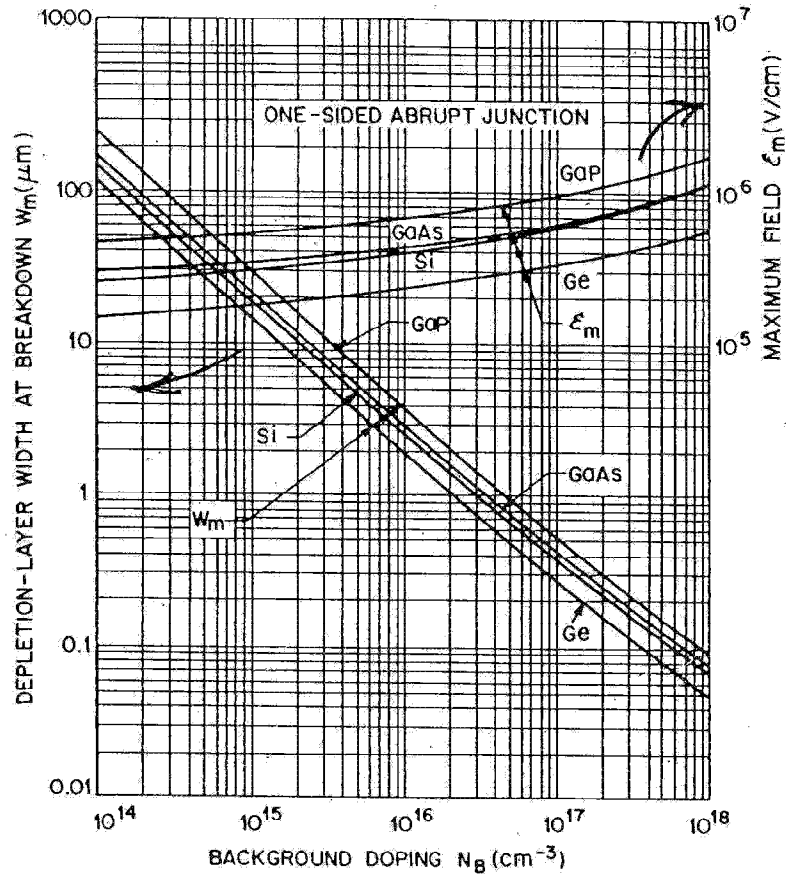


Fig. 29 Depletion-layer width and maximum field at breakdown for one-sided abrupt junctions in Ge, Si, <100>-oriented GaAs, and GaP. (After Sze and Gibbons, Ref. 35.)

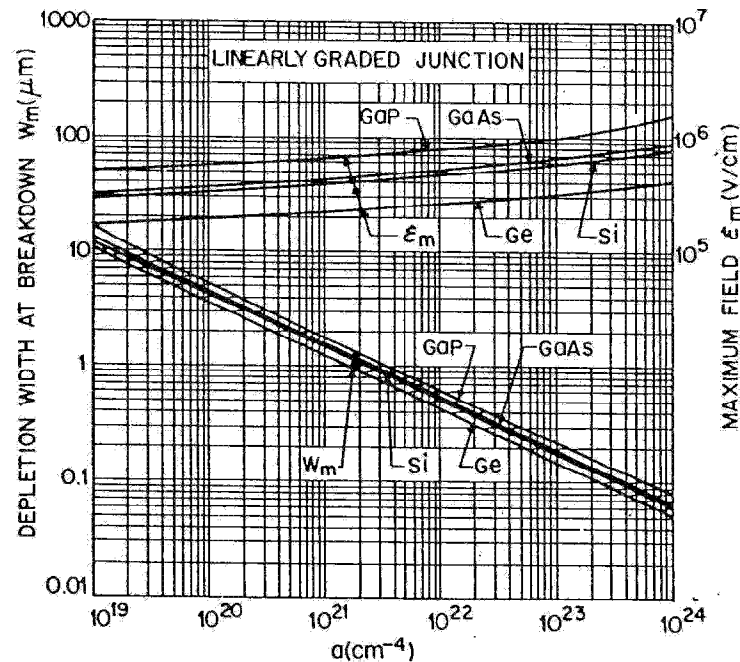


Fig. 30 Depletion-layer width and maximum field at breakdown for linearly graded junctions in Ge, Si, <100>-oriented GaAs, and GaP. (After Sze and Gibbons, Ref. 35.)

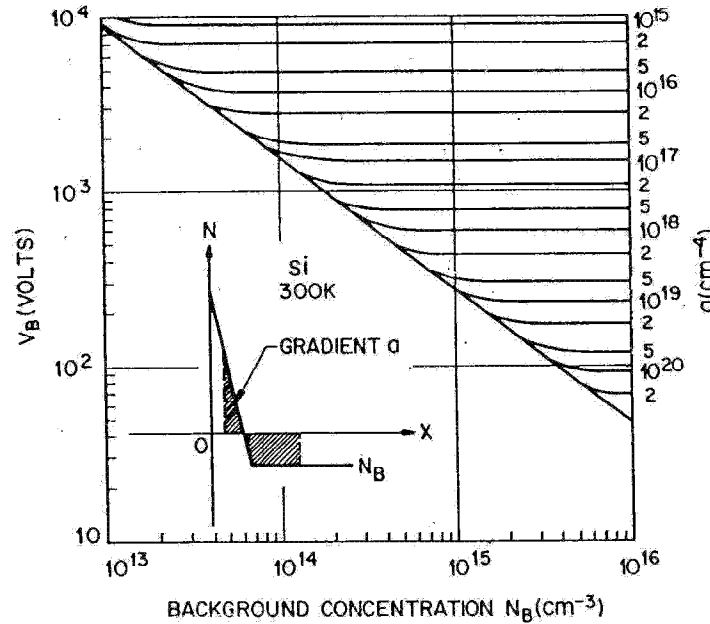


Fig. 31 Breakdown voltage for diffused junctions. The insert shows the space-charge distribution. (After Ghandhi, Ref. 39.)

An approximate universal expression can be given as follows for the results above comprising all semiconductors studied:

$$V_B \cong 60(E_g/1.1)^{3/2}(N_B/10^{16})^{-3/4} \quad \text{V} \quad (79a)$$

for abrupt junctions where E_g is the room-temperature bandgap in eV, and N_B is the background doping in cm^{-3} ; and

$$V_B \cong 60(E_g/1.1)^{6/5}(a/3 \times 10^{20})^{-2/5} \quad \text{V} \quad (79b)$$

for linearly graded junctions where a is the impurity gradient in cm^{-4} .

For diffused junctions with a linear gradient on one side of the junction and a constant doping on the other side (shown in Fig. 31, insert), the breakdown voltage lies between the two limiting cases considered previously³⁹ (Figs. 26 and 28). For large a and low N_B , the breakdown voltage of diffused junctions (Fig. 31) is given by the abrupt junction results (bottom line); on the other hand, for small a and high N_B , V_B will be given by the linearly graded junction results (parallel lines).

In Figs. 26 through 30, it is assumed that the semiconductor layer is thick enough to support the depletion-layer width W_m at breakdown (Fig. 29). If, however, the semiconductor layer W is smaller than W_m (shown in Fig. 32, insert), the device will be punched through (i.e., the depletion layer reaches the $n-n^+$ interface) prior to breakdown. As the reverse bias increases further, the device will eventually break down. The maximum electric field \mathcal{E}_m is essentially the same as for the non-punched-through diode. Therefore, the breakdown voltage V_{PT} for the punched-through diode can be

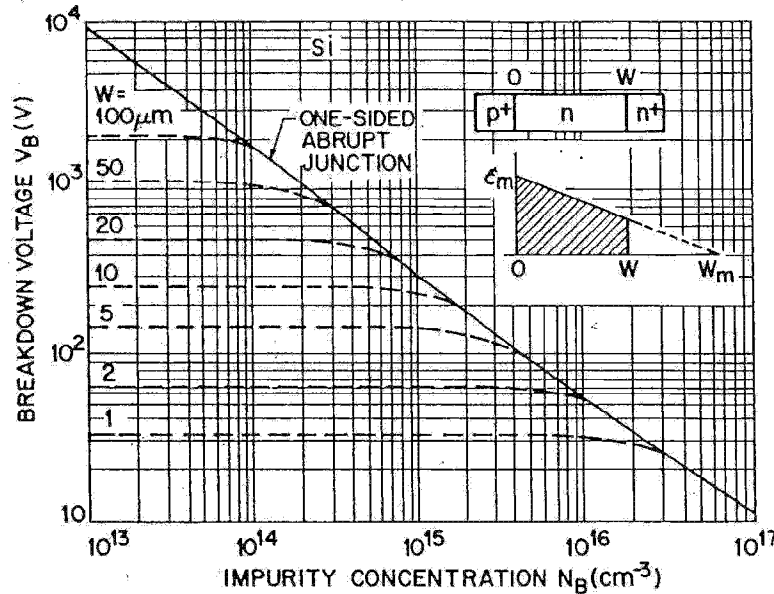


Fig. 32 Breakdown voltage for $p^+-\pi-n^+$ and $p^+-\nu-n^+$ junctions, where π is for lightly doped p -type and ν for lightly doped n -type. W is the thickness of the π or ν region.

given by

$$\frac{V_{PT}}{V_B} = \frac{\text{shaded area in Fig. 32 insert}}{(\epsilon_m W_m)/2} = \left(\frac{W}{W_m}\right)\left(2 - \frac{W}{W_m}\right). \quad (80)$$

The punch-through usually occurs when the doping concentration N_B becomes sufficiently low as in a $p^+-\pi-n^+$ or an $p^+-\nu-n^+$ diode, where π stands for a lightly doped p -type and ν for a lightly doped n -type semiconductor. The breakdown voltages for such diodes as calculated from Eq. 80 are shown in Fig. 32 as a function of the background doping for Si one-sided abrupt junction formed on epitaxial substrates (e.g., ν on n^+ with the epitaxial-layer thickness W as a parameter). For a given thickness, the breakdown voltage approaches a constant value as the doping decreases, corresponding to the punch-through of the epitaxial layer.

The results in Figs. 26 through 32 are for avalanche breakdowns at room temperature. At higher temperatures the breakdown voltage increases. A simple explanation of this increase is that hot carriers passing through the depletion layer under a high field lose part of their energy to optical phonons after traveling each electron-phonon mean free path λ . The value of λ decreases with increasing temperature, (Eq. 84 of Chapter 1). Therefore, the carriers lose more energy to the crystal lattice along a given distance at constant field. Hence the carriers must pass through a greater potential difference (or higher voltage) before they can acquire sufficient energy to generate an electron-hole pair. The detailed calculations have

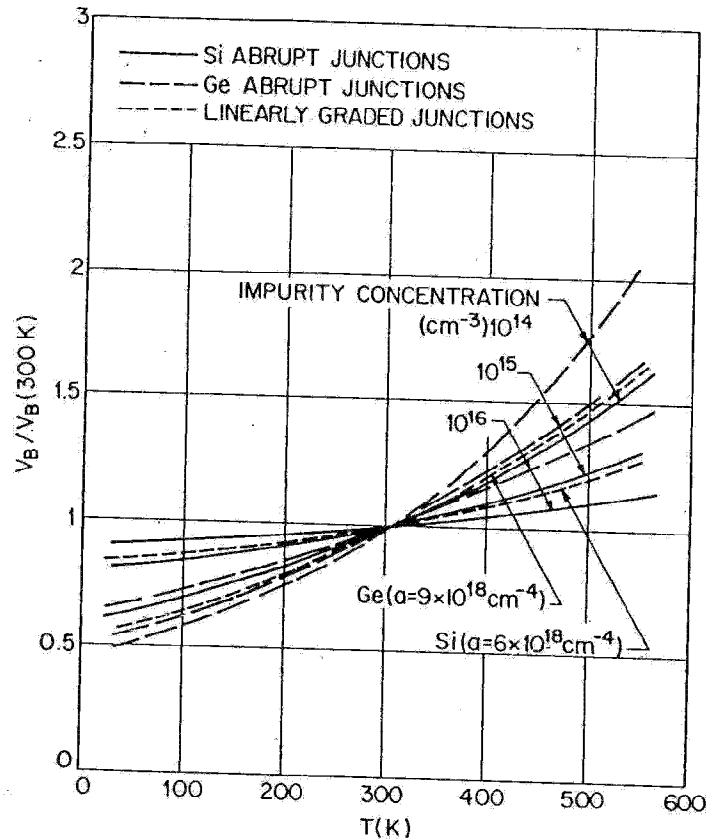


Fig. 33 Normalized avalanche breakdown voltage versus lattice temperature. The breakdown voltage increases with temperature. (After Crowell and Sze, Ref. 40.)

been done by the use of a modification of Baraff's theory⁴⁰ as discussed in Chapter 1. The predicted values of V_B normalized to the room-temperature value are shown in Fig. 33 for Ge and Si. For the same doping profile, the predicted percentage change on V_B with temperature is about the same for GaAs as it is for Ge and for GaP as it is for Si junctions. Note that there are substantial increases of the breakdown voltage, especially for lower dopings (or small gradient) at higher temperatures.⁴¹ Figure 34 shows the measured results,⁴² which agree quite well with this theory.

For planar junctions, the very important junction curvature effect should be considered. A schematic diagram of a planar junction has been shown in Fig. 9b. Since the cylindrical and/or spherical regions of the junction have a higher field intensity, the avalanche breakdown voltage is determined by these regions. The potential $V(r)$ and the electric field $\mathcal{E}(r)$ in a cylindrical or spherical p-n junction can be calculated from Poisson's equation:

$$\frac{1}{r^n} \frac{d}{dr} [r^n \mathcal{E}(r)] = \frac{\rho(r)}{\epsilon_s} \quad (81)$$

where n equals 1 for the cylindrical junction, and 2 for the spherical

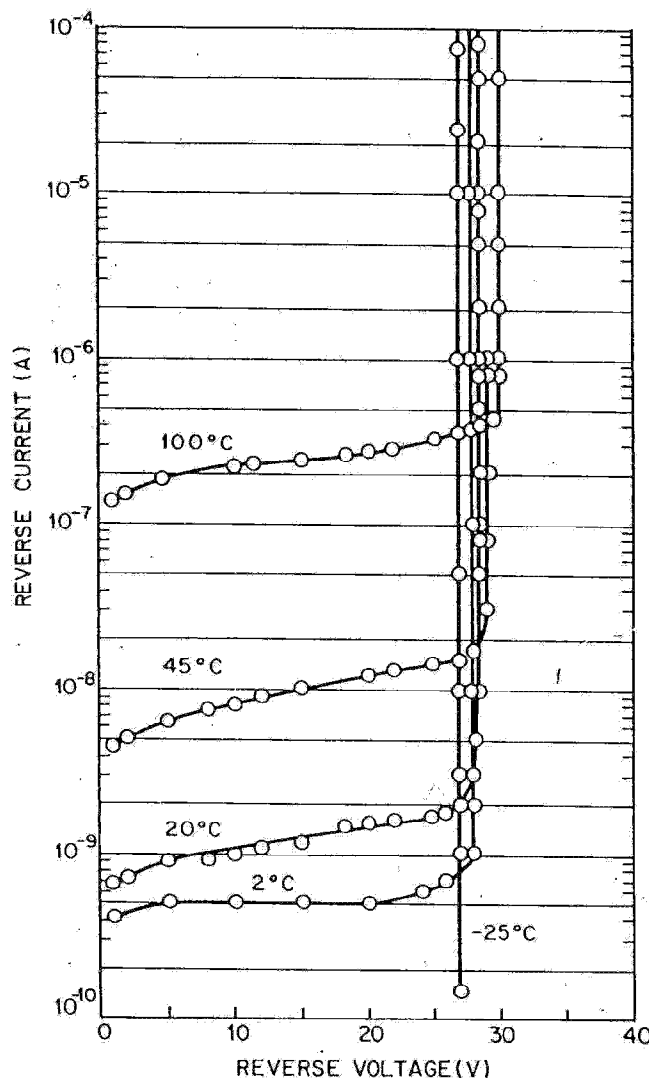


Fig. 34 Temperature dependence of reverse I - V characteristics of a microplasma-free n^+ - p Si diode with $N_B = 2.5 \times 10^{16} \text{ cm}^{-3}$ and an n -type guard ring. The temperature coefficient is $0.024 \text{ V/}^\circ\text{C}$. (After Goetzberger et al., Ref. 42.)

junction. The solution for $\mathcal{E}(r)$ can be obtained from Eq. 81 and is given by

$$\mathcal{E}(r) = \frac{1}{\epsilon_s r^n} \int_{r_j}^r r^n \rho(r) dr + \frac{\text{constant}}{r^n} \quad (82)$$

where r_j is the radius of curvature of the metallurgical junction, and the constant must be adjusted so that the breakdown condition Eq. 74 or 75 is satisfied.

The calculated results for Si one-sided abrupt junctions at 300 K can be expressed by simple analytical equations:³⁹

$$\frac{V_{CY}}{V_B} = \left[\frac{1}{2} (\eta^2 + 2\eta^{6/7}) \ln(1 + 2\eta^{-8/7}) - \eta^{6/7} \right] \quad (83)$$

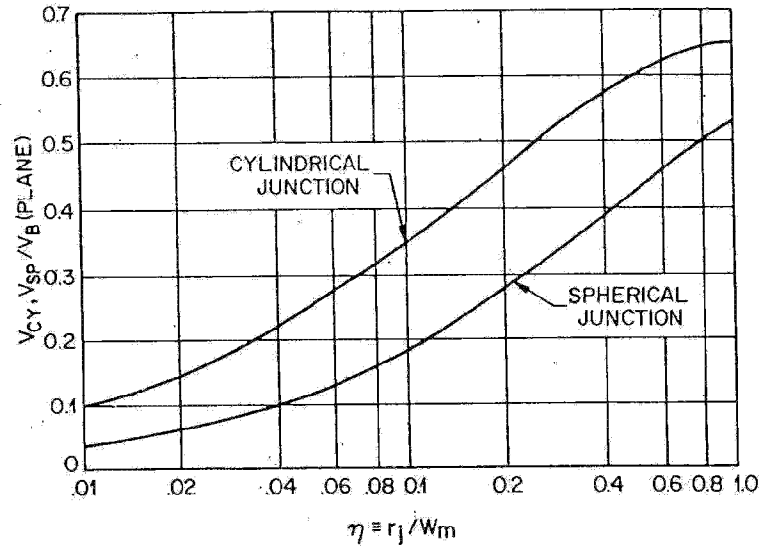


Fig. 35 Normalized breakdown voltage of cylindrical and spherical junction as a function of the normalized radius of curvature. (After Ghandhi, Ref. 39.)

for cylindrical junctions, and

$$\frac{V_{SP}}{V_B} = [\eta^2 + 2.14\eta^{6/7} - (\eta^3 + 3\eta^{13/7})^{2/3}] \quad (84)$$

for spherical junctions, where V_{CY} and V_{SP} are the breakdown voltages of cylindrical and spherical junctions, respectively, V_B is the breakdown voltage of a plane junction having the same background doping, and $\eta \equiv r_j / W_m$. Figure 35 illustrates the breakdown voltages for cylindrical and spherical abrupt junctions as a function of η . Clearly, as the radius of curvature becomes smaller, so does the breakdown voltage. For linearly graded cylindrical or spherical junctions, the calculated results show that the breakdown voltage is relatively independent of its radius of curvature.²⁵

2.6 TRANSIENT BEHAVIOR AND NOISE

2.6.1 Transient Behavior

For switching applications the transition from forward bias to reverse bias must be nearly abrupt and the transient time short. In Fig. 36a a simple circuit is shown where a forward current I_F is flowing in the p-n junction; at time $t = 0$, the switch S is suddenly thrown to the right, and initial reverse current $I_R \approx V/R$ flows. The transient time is defined as the time in which the current reaches 10% of the initial current I_R , and is equal to the sum of t_1 and t_2 as shown in Fig. 36b, where t_1 and t_2 are the time intervals for the constant-current phase and the decay phase, respectively. Consider